Numerical Simulation of Mountain Waves over the Southern Andes. Part I: Mountain Wave and Secondary Wave Character, Evolutions, and Breaking

Thomas S. Lund,[a] David C. Fritts,[a,b] Kam Wan,[a] Brian Laughman,[a,d] and Han-Li Liu[c]

[a] GATS Inc., Boulder, Colorado
[b] Embry-Riddle Aeronautical University, Daytona Beach, Florida
[c] HAO, NCAR, Boulder, Colorado

ABSTRACT: This paper addresses the compressible nonlinear dynamics accompanying increasing mountain wave (MW) forcing over the southern Andes and propagation into the mesosphere and lower thermosphere (MLT) under winter conditions. A stretched grid provides very high resolution of the MW dynamics in a large computational domain. A slow increase of cross-mountain winds enables MWs to initially break in the mesosphere and extend to lower and higher altitudes thereafter. MW structure and breaking is strongly modulated by static mean and semidiurnal tide fields exhibiting a critical level at ~114 km for zonal MW propagation. Varying vertical group velocities for different zonal wavelengths λ_x yield initial breaking in the lee of the major Andes peaks for $\lambda_x \sim 50$ km, and extending significantly upstream for larger λ_x approaching the critical level at later times. The localized extent of the Andes terrain in latitude leads to "ship wave" responses above the individual peaks at earlier times, and a much larger ship-wave response at 100 km and above as the larger-scale MWs achieve large amplitudes. Other responses above regions of MW breaking include large-scale secondary gravity waves and acoustic waves that achieve very large amplitudes extending well into the thermosphere. MW breaking also causes momentum deposition that yields local decelerations initially, which merge and extend horizontally thereafter and persist throughout the event. Companion papers examine the associated momentum fluxes, mean-flow evolution, gravity wave–tidal interactions, and the MW instability dynamics and sources of secondary gravity waves and acoustic waves.

KEYWORDS: Atmosphere-land interaction; Buoyancy; Gravity waves; Instability; Mountain waves; Turbulence

1. Introduction

Mountain waves (MWs) have been the subject of numerous observational, modeling, and theoretical studies over the previous 100 years (Smith 2018). Examples of important physical effects include downslope winds, turbulence at flight altitudes, and transport and deposition of energy and momentum that have major roles in weather, climate, and atmospheric composition and structure. An extensive literature has addressed their dynamics and implications extending into the middle stratosphere and spawned many reviews and books. Only recently, however, were MWs first observed in the mesosphere over the central Andes (Smith et al. 2009), though modeling studies anticipated this potential (Schoeberl 1985; Bacmeister 1993; Sato et al. 2009) and motivated earlier measurement programs (Goldberg et al. 2006).

MWs have been understood to play major roles in atmospheric circulation, structure, and variability at lower altitudes for many years. As such, many efforts have addressed their parameterization at lower altitudes (see Palmer et al. 1986; Lott 1999) and as a component of more general gravity wave (GW) parameterizations throughout the atmosphere (Kim et al. 2003). Importantly, global measurements cannot resolve GW λ_h smaller than ~200–400 km (Geller et al. 2013), hence cannot include potentially significant contributions by GWs having $\lambda_h \sim$ 30–200 km. In situ measurements, in contrast, emphasize the importance of intermittent MW contributions at typically much smaller λ_h (Hertzog et al. 2008). Observational studies performed to date, by MWs having $\lambda_h \sim$ 30–100 km (Bossert et al. 2018; Fritts et al. 2018) and those specifically focused on MW momentum fluxes in the mesosphere and lower thermosphere (MLT), likewise suggest that the major momentum fluxes are contributed.

Since their discovery at high altitudes, increasing attention has focused on the conditions leading to MW responses in the MLT and their associated dynamics. The majority of recent studies resulted from the Deep Propagating Gravity Wave Experiment (DEEPWAVE) involving airborne measurements over and around the New Zealand South Island (SI) in June and July 2014. These were supported by extensive ground-based and radiosonde measurements on SI and Tasmania spanning a broader interval [see the DEEPWAVE overview by Fritts et al. (2016)]. DEEPWAVE was preformed in the Southern Hemisphere in order to avoid the potential for a sudden stratospheric warming, one of which induced a MW critical level that prevented propagation into the MLT during the January 2003 Mountain and Convective Waves Ascending Vertically (MaCWAVE) program in northern Sweden (Goldberg et al. 2006; Wang et al. 2006). The initial target was intended to be the southern Andes because of their dominant contributions to GW variances in the middle stratosphere (see Hendricks et al. 2014), but DEEPWAVE was moved to

New Zealand due to an inability to identify a suitable wintertime aircraft base near the tip of South America.

The comprehensive DEEPWAVE dataset has enabled studies of multiple aspects of MW dynamics from their sources into the MLT to date. Observations in the upper troposphere and lower stratosphere employing flight-level in situ measurements revealed the character and diversity of MW responses spanning many research flights. These data were employed by Smith et al. (2016) and Fritts et al. (2018) to assess MW wavelengths, amplitudes, vertically propagating versus trapped lee wave character, and energy and momentum fluxes for variable forcing conditions. Kruse et al. (2016) and Bramberger et al. (2017) addressed the conditions enabling MW propagation into the stratosphere. Propagation conditions enabling MWs to penetrate to high altitudes were examined by Kaifler et al. (2015), Bramberger et al. (2017), and Fritts et al. (2018). Studies by Fritts et al. (2018) and Portele et al. (2018) identified the causes for sometimes significant delays between variable MW forcing and responses in the stratosphere and MLT. One such case in which MWs arose due to flow over the low terrain of the Auckland Islands was found to generate a lee "ship wave" response exhibiting MW breaking extending above 80 km (Eckermann et al. 2016; Pautet et al. 2016; Broutman et al. 2017). Secondary GWs (SGWs) in the stratosphere and MLT were observed at smaller scales and accompanied MW breaking at lower altitudes (Bossert et al. 2015, 2017). Large-amplitude MW breaking and large momentum fluxes in the mesosphere were seen to accompany weak forcing, but conducive propagation conditions at lower altitudes (Heale et al. 2017; Bossert et al. 2018; Fritts et al. 2018; Taylor et al. 2019). In addition, the radar studies of de Wit et al. (2017) suggest that the large eastward GW momentum flux observed above the stratospheric jet is likely due to secondary waves resulting from MW breaking over the southern Andes. DEEPWAVE airborne observations also provided evidence of trailing waves refracting into the polar vortex in the stratosphere (Jiang et al. 2019). Finally, ground-based measurements at the Andes Lidar Observatory at 30°S and during DEEPWAVE enabled identification of the instability dynamics accounting for MW breaking in the MLT in two events (Hecht et al. 2018; Fritts et al. 2019a).

Modeling and data analyses described in several of the DEEPWAVE studies cited above have revealed the complexity of MW responses to variable wind and temperature fields at all altitudes. None of the modeling efforts extended to the highest altitudes observed, however, nor did they resolve the instability dynamics accounting for MW breaking, dissipation, and SGW generation. As such, they were unable to describe the true variability of the responses, which likely include the intermittency and scales of SGWs, influences of instability dynamics on the variability of MW amplitudes in space and time, and details of their interactions with mean and tidal fields throughout the atmosphere. DEEPWAVE studies to date also provided no information on the potential impacts at higher altitudes in the thermosphere, though observations over New Zealand in March 2009 revealed SGWs penetrating to ~250 km (Smith et al. 2013).

To address these dynamics comprehensively, we have performed a numerical simulation of MW generation and responses extending to 200 km in a large computational domain, but having very high spatial resolution in the central portion where MW breaking and SGW generation are anticipated. Because the largest responses in the stratosphere accompany MW forcing over the southern Andes and the strongest polar vortex winds enabling deep MW penetration occur at higher southern latitudes, we chose to perform this initial simulation over the southern Andes rather than over New Zealand. We anticipate future simulations targeting New Zealand to allow comparisons with specific DEEPWAVE events.

Our goals in this paper are to describe the MW and related dynamics accompanying strong flow over the southern Andes extending into the MLT under winter conditions allowing deep MW propagation. Section 2 describes the model and the simulation configuration employed. The evolution of the MW field over ~4 h following a gradual ramp in cross-mountain flow is presented in section 3. Key elements of the response include 1) strong MW breaking extending from the stratosphere to the lower thermosphere, 2) excitation and evolution of SGWs and acoustic waves (AWs) penetrating to high altitudes, and 3) filtering and modulation of the MW and SGW field by tidal winds. Section 4 provides a discussion of these results relative to previous studies. Our summary and conclusions are presented in section 5. Companion papers by Fritts et al. (2019b, manuscript submitted to *J. Atmos. Sci.*, hereafter F19b; D. C. Fritts et al. 2020, unpublished manuscript, hereafter F20) describe the momentum fluxes, mean-flow accelerations, and GW–tidal interactions and the MW instability dynamics and sources of SGWs and AWs, respectively.

2. Model description and setup

a. Governing equations

We start with the compressible Navier–Stokes equations, written in strong conservation law (divergence) form:

$$\frac{\partial \rho}{\partial t} + \frac{\partial \rho u_j}{\partial x_j} = 0, \tag{1}$$

$$\frac{\partial \rho u_i}{\partial t} + \frac{\partial \rho u_i u_j}{\partial x_j} = -\frac{\partial p}{\partial x_i} - \rho g \delta_{i3} + \frac{\partial \sigma_{ij}}{\partial x_j}, \tag{2}$$

$$\frac{\partial \rho E}{\partial t} + \frac{\partial (\rho E + p) u_j}{\partial x_j} = -\rho g u_3 + \frac{\partial u_i \sigma_{ij}}{\partial x_j} - \frac{\partial q_j}{\partial x_j}, \tag{3}$$

where σ_{ij} and q_j are the viscous stress and thermal conduction, defined as

$$\sigma_{ij} = \mu \left[\left(\frac{\partial u_i}{\partial x_j} + \frac{\partial u_j}{\partial x_i} \right) - \frac{2}{3} \left(\frac{\partial u_k}{\partial x_k} \right) \delta_{ij} \right], \tag{4}$$

$$q_j = -\kappa \frac{\partial T}{\partial x_j}, \tag{5}$$

and where μ is the dynamic viscosity, κ is the thermal conductivity, and δ_{ij} is the Kronecker delta. Here both μ and κ are the sums of molecular and subgrid-scale components, where

the molecular components depend only on the temperature through Sutherland's law (White1974), and where the turbulent components are estimated via the dynamic subgrid-scale model (see section 2f below).

The solution variables are the density ρ, the momentum per unit volume ρu_i or (ρu, ρv, ρw), and the total energy per unit volume $\rho E = \rho(e + u_k u_k/2) = \rho(c_v T + u_k u_k/2)$. The three coordinate directions are (i, j, k) or (x, y, z). Here $c_v = R/(\gamma - 1)$ is the specific heat at constant volume and T is the temperature. We assume the atmosphere is of fixed composition with constant values of the gas constant, $R = 287\,\mathrm{J\,kg^{-1}\,K^{-1}}$, and the specific heat ratio, $\gamma = 1.4$. This step should be viewed as an approximation as R increases significantly with altitude especially above 120 km (Vadas 2007). As shown later in the paper, instabilities are largely constrained below 120 km, where R and γ vary by less than 7% (Vadas 2007; Lund and Fritts 2012). The pressure p appears as an auxiliary variable and it is related to the density and temperature through the ideal gas law:

$$p = \rho R T. \qquad (6)$$

b. Finite-volume solution method

The governing equations are discretized using the finite-volume framework, in which each computational cell is considered to be a small control volume. Our method, known as the Complex Geometry Compressible Atmospheric Model (CGCAM) is designed for fully curvilinear meshes, which is necessary for our detailed terrain-following description of the Andes mountain ranges.

In CGCAM the solution variables are stored at the cell centroids and fluxes on the faces are constructed using a kinetic energy–conserving interpolation scheme similar to that discussed in Felten and Lund (2006) for the incompressible Navier–Stokes equations. Several similar compressible finite-volume algorithms can be found in the literature, e.g., Hou and Mahesh (2005), Shoeybi et al.(2010), Reiss and Sesterhenn (2014), and Coppola et al. (2019) and a more complete description of our scheme can be found in Dong et al. (2019).

The resulting scheme is globally conservative for mass, momentum, total energy, and kinetic energy. Time advancement is achieved via a low-storage, third-order accurate Runge–Kutta scheme with a fixed time step of $\Delta t = 0.3\,\mathrm{s}$.

c. Simulation domain and grid layout

The computational domain extends 2500 (2000) km in longitude (latitude) and 200 km in altitude. It is centered at 48.2°S, 73.5°W between the two major massifs of the southern Andes, each of which has maximum terrain height ~4 km. The high-resolution, central portion of the domain extends 250 (750) km in longitude (latitude), is centered 75 km east of the major massifs, and has horizontal resolution of 500 m and vertical resolution of 500 m below 144 km. Outside of the high-resolution region the horizontal grid spacing is increased gradually via a fixed 2% stretching rate in order to achieve ~22 km spacing at the zonal boundary and ~12 km at the meridional boundary. Although the mesh is considerably coarser near the horizontal boundaries, it is still sufficient to

resolve the predominantly large-scale waves found in this region (see section 3). The vertical mesh is likewise stretched above 144 km to a resolution of 1.4 km at 200 km altitude. A total of 900 × 1840 × 352 mesh points are used in the zonal, meridional, and vertical directions, respectively.

A series of two-dimensional simulations at resolutions of 2000, 1000, 500, and 250 m for a cross-section passing over the South Peak was used to form a mesh-convergence study. As expected, the difference between successive solutions decreased with resolution and the changes between 500 and 250 m were sufficiently small that the 500 m spacing was deemed adequate for resolving the MW dynamics.

The southern Andes terrain is obtained from the NOAA Global Land One-km Base Elevation Project (GLOBE) dataset (Hastings et al. 1999). The terrain at the north end of the domain is artificially damped to sea level via a hyperbolic tangent function with characteristic width of 100 km, centered 300 km from the boundary. This modification eliminates surface forcing near the north boundary, making it possible to use a relatively simple boundary condition there (see discussion below). The terrain and the computational mesh in the horizontal are shown in Fig. 1a. While the mesh uses a Cartesian layout in the horizontal directions, it is distorted in the vertical direction in order to match the terrain at the lower boundary. The vertical mesh distortions are then gradually faded out with increasing grid level, becoming nonexistent at the 30th level (15 km altitude). The mesh is then purely Cartesian from this position to the top of the domain.

Terrain elevations and zonal wavelength spectra over the northern and southern massifs 120 km north (N) and 120 km south (S) of the domain center averaged over 30 km in latitude are shown in Figs. 1b and 1c. The spectra reveal power at zonal wavelengths $\lambda_x \sim$ 25–200 km, with multiple peaks near 40, 80, and 160 km for the N Peak and a single broad peak near 70 km for the S Peak. As shown in section 3, the major GW responses at later times occur close to these values, mainly within the range $\lambda_x \sim$ 30–200 km.

d. Boundary conditions

Since our focus is on GW excitation and evolution, we choose not to resolve the surface boundary layer and instead employ no slip and adiabatic boundary conditions at the terrain surface. This step drastically reduces the number of mesh points required near the surface thus allowing us to cluster the bulk of the points at the upper altitudes where instability and wave breaking occur. From a GW perspective, the main effect of the boundary layer is an adjustment of the effective terrain shape due to its displacement effect, and perhaps local regions of separated flow behind steep leeward ridges (e.g., Jiang et al. 2007). These are difficult features to predict without a fine near-surface grid and an accurate turbulence model, however, and thus we have not resorted to any much more approximate techniques in order to account for these effects. We do believe, however, that viscous effects play a rather minor role in GW excitation. For example, the displacement thickness of a turbulent boundary layer is roughly one-eighth of its overall thickness (White 1974) and thus a 1 km deep boundary layer will have a displacement thickness of approximately 125 m,
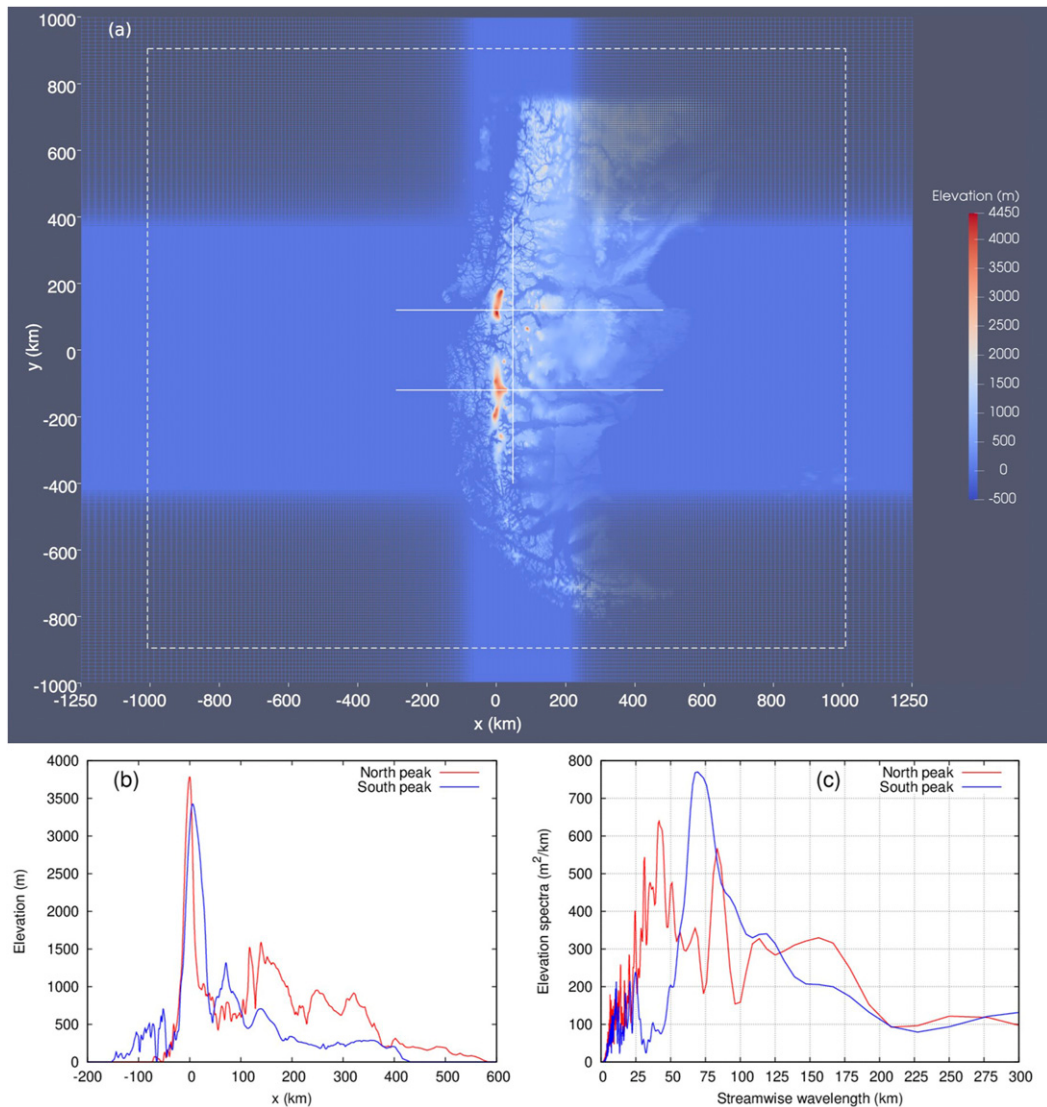
FIG. 1. (a) Southern Andes topography and CGCAM domain and mesh and (b) terrain elevations and (c) spectra over the north and south peaks. The 500-m mesh extends from −50 to 200 km in x and from ±400 km in y. The solid lines in (a) show the locations of the cross sections shown in the figures below, while the dashed rectangle shows the central region without sponge-layer damping.

which is small compared with Andes mountain terrain heights in excess of 4000 m. It should be noted that neglect of the boundary layer will preclude baroclinic vorticity generation associated with lee vortices (Smolarkiewicz and Rotunno 1989, 1990) and will also preclude diabatic cooling over ice sheets that enhances MW amplitudes over wide terrain (Doyle et al. 2005). In addition, Leutbecher and Volkert (2000) have shown that the computed wave amplitude is sensitive to level of surface friction present in the simulation. Numerical sponge layers are used at the upper and horizontal boundaries in order to absorb outgoing GW and AWs. The layers are 200 km wide at the zonal boundaries, 100 km wide at the meridional boundaries, and 15 km deep at the upper boundary. (The position of the sponge layers is shown with a dashed lined in Fig. 1a.)

The sponges are implemented as "noise canceling" forcing terms added to each of the conservation equations. For example, within the interval $x_b − x_w \leq x \leq x_b$, the momentum equation is modified via

$$\frac{d\rho u_i}{dt} = \cdots - \left\{ 1 + \tanh\left[2.5\left(\frac{x - x_b}{x_w}\right) \right] \middle/ \tanh(2.5) \right\}\left(\frac{\rho u_i - \overline{\rho}\, \overline{u_i}}{\tau_s}\right), \quad (7)$$

where $\overline{\rho}$ and $\overline{u_i}$ are the background density and background wind, x_b is the position of the right boundary, x_w is the sponge width, and τ_s is its time constant. The hyperbolic tangent function provides a smooth weighting function that transitions between zero at $x = x_b − x_w$ and 1.0 at $x = x_b$. A simple analysis

of the above equation shows that it drives a fluctuation $\rho u_i - \overline{\rho}\,\overline{u_i}$ to zero exponentially with time constant τ_s. If one absorbs the tanh weighting function into an effective time constant, then the sponge layer can be viewed as an exponential damping zone with time constant that decreases with distance for waves attempting to pass through. This construction allows for gradual attenuation of incident waves, resulting in near complete extinction at the boundary with negligible reflected wave energy. The time constant τ_s is set to 1.0 s, or $3.33\Delta t$.

Conventional boundary conditions must also be used with the sponges and we use periodic conditions in the horizontal directions and a characteristic outflow condition at the upper boundary for this purpose. While periodic boundary conditions in the horizontal directions would seem to be a poor choice, the sponges effectively transform these into inflow/outflow/radiation conditions. To see that this is so, consider an advecting flow disturbance or a right-running GW approaching the downstream boundary. This disturbance will be attenuated to near extinction as it attempts to cross the sponge layer, leaving little or no disturbance at the downstream boundary. Due to the periodic boundary condition any small residual arriving at the boundary will of course reenter the domain on the left, but will then encounter the sponge layer on that side, diminishing its amplitude even further as it attempts to propagate across it. The net result is that outgoing waves simply appear to leave the domain permanently once they enter the sponge region. Similarly flow structures advecting toward an outflow boundary appear to leave the domain permanently while disturbance-free flow at the specified background conditions is supplied at the downstream end of the sponge region at an inflow boundary. We have found the sponge approach to be far superior at eliminating wave reflections as compared with even sophisticated radiation conditions that act strictly at the boundary.

The only downside of the sponge layers is that they increase the cost of the simulation. Since the sponge terms are nonphysical, the solution cannot be used anywhere within the sponge regions. This reality means that the effective position of the boundaries must be moved inward by the thickness of the sponge, thereby reducing the valid flow region. In our case, this requirement leads to an effective domain that extends from −1050 to 1050 km in the zonal direction, from −900 to 900 km in the meridional direction, and from 0 to 185 km in z. We respect these restricted domain limits for all analysis of our results and never display data taken from within a sponge region.

e. Initial conditions and forcing

Background fields for the Andes MW simulation were obtained from a Whole Atmosphere Community Climate Model (WACCM) simulation for July conditions. This WACCM version is based on a spectral element (SE) dynamical core solved on a cubed sphere, with a global quasi-uniform horizontal resolution of ~25 km. The vertical domain extends from the ground to ~145 km, with vertical resolution of 0.1 scale height above the middle stratosphere and higher below. The model can resolve GWs having $\lambda_x \sim 200$ km and larger.

A detailed description of WACCM and the simulation employed here can be found in Liu et al. (2014) and Liu (2016). The wind and temperature fields at 50°S, 65°W at the time selected had a strong eastward jet at ~50 km and significant tidal influences at higher altitudes. Above 120 km, the winds were specified to approximate tidal winds asymptotically approaching $U_0 = 0$ and $V_0 = 70$ m s^{-1} above 200 km to allow exploration of SGWs and AWs arising from MW dynamics at lower altitudes without constraints by large zonal wind shears at higher altitudes. Initial profiles of U_0, V_0, temperature $T_0(z)$, and the corresponding $N_0^2(z)$ profile (for initial mean buoyancy frequency N_0) are shown in Figs. 2a, 2b, and 2d.

These fields were assumed to be uniform over the domain, as the major responses of interest are confined to about ±5° in longitude and latitude around the domain center. They were also assumed to be constant in time, apart from departures driven by MW forcing. This is because MW propagation from ~10 to 80 km occurs on short time scales because strong zonal winds cause the dominant MW $\lambda_x \sim 30$–80 km to have $\lambda_z \sim 15$–60 km or larger, and hence to be nonhydrostatic and have large vertical group velocities c_{gz}. As a result, the dynamics of interest occur on time scales significantly shorter than tidal periods.

To simulate the buildup of a strong MW event, the mean winds were initially damped toward zero below an altitude of ~25 km and were then gradually increased in time toward the target $U_0(z)$ and $V_0(z)$ profiles via

$$[U, V](z, t) = [U, V]_0(z)\{d(z) + [1 - d(z)]f(t)\}, \quad (8)$$

where

$$d(z) = \frac{1}{2}\left\{1 + \tanh\left[\frac{z - z_c}{z_w}\right]\right\}, \quad (9)$$

$$f(t) = \min\left[\frac{1}{2}\left\{1 + \tanh\left[\frac{t - t_m}{t_m/3}\right]\right\}\bigg/ \tanh(3)\right\}, 1\right], \quad (10)$$

and where $t_m = 6$ h, $z_c = 22$ km, and $z_w = 4$ km. The damping function $d(z)$ decreases the initial winds very close to zero below 10 km and this effect is shown by the thin line near the bottom of Fig. 2b. The ramp function $f(t)$, shown in Fig. 2c, increases the winds smoothly over a total duration of 12 h. The central (most rapid) portion of the ramp has a rate equal to that of a 4 h linear ramp.

Because the imposed mean and tidal wind and stability profiles are highly structured in altitude, the initial mean Richardson number, $\mathrm{Ri}(z) = N_0^2[(dU_0/dz)^2 + (dV_0/dz)^2]$, can have very small values; see Fig. 2e. This reveals several altitudes at which $\mathrm{Ri} \sim 0.5$–2 from $z = 80$–115 km where mean shears may contribute to instabilities induced by MWs or SGWs.

GW breaking results in local momentum deposition and flow accelerations that cause the local mean winds (U, V, W) and altered stability N to evolve in space and time, though W will always be small on larger spatial scales. The mean variations influence the propagation, structure, and orientations of GWs in, and encountering, these environments. To describe these influences in our discussion below, we express MW or
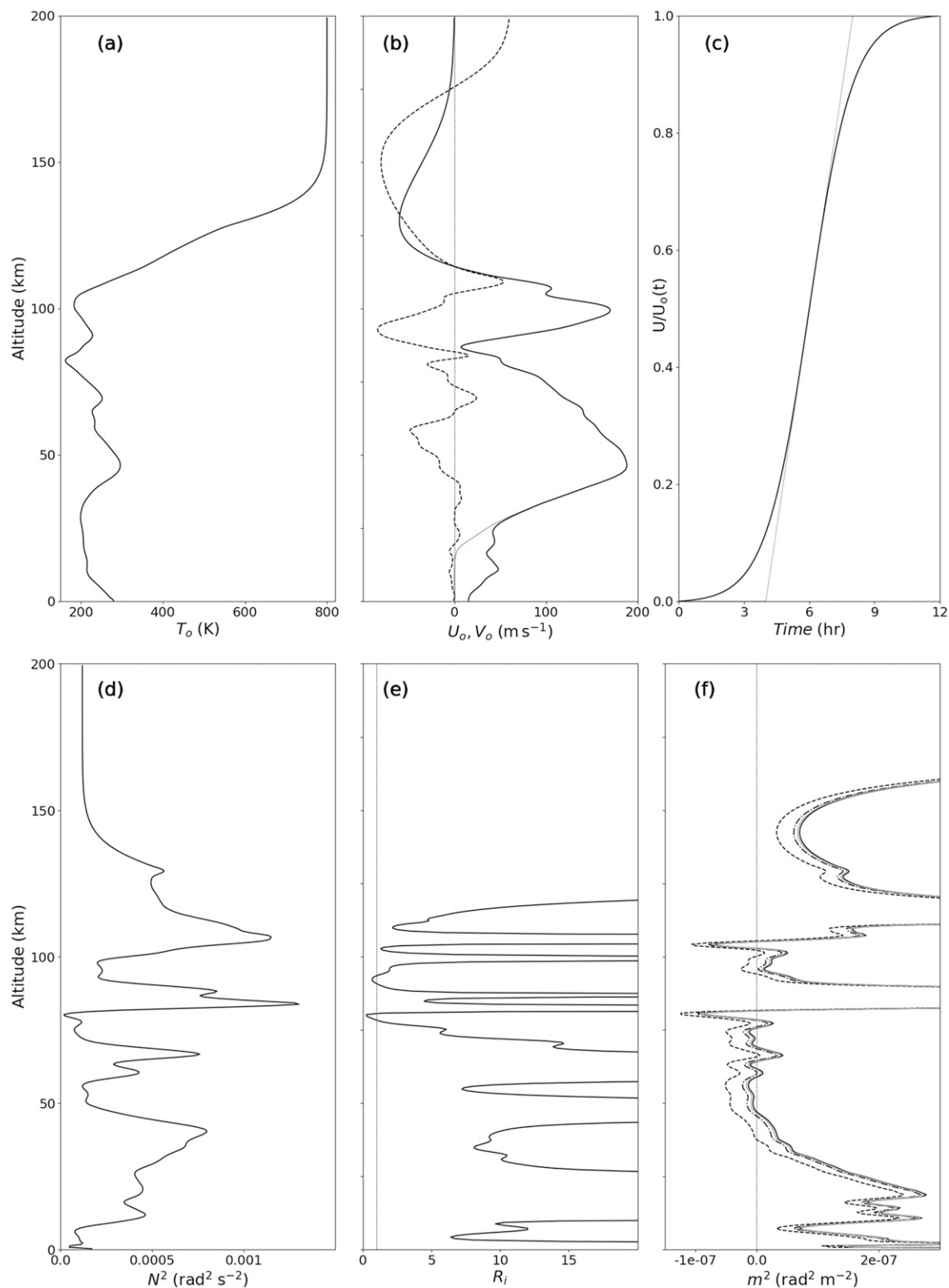
FIG. 2. Initial profiles of T_0, U_0 and V_0, time, N_0^2, Ri, m^2, and the forcing ramp. The thin line in (b) shows the initial U_0. The m^2 are shown for $\lambda_h = 30$, 50, and 80 km.

SGW intrinsic character in the vertical plane of GW propagation having horizontal mean wind U_h assumed largely toward east. Then the intrinsic phase speed and intrinsic frequency are $c_i = (c - U_h)$ and $\omega_i = k_h c_i$ for GW phase speed c along U_h, horizontal and vertical wavenumbers are $k_h = 2\pi/\lambda_h$ and $m = 2\pi/\lambda_z$, and m^2 is given by

$$m^2 = \frac{N^2}{(U_h - c)^2} - \frac{U_{hzz}}{(U_h - c)} + \frac{U_{hz}}{[(U_h - c)H]} - k_h^2 - \frac{1}{4H^2}. \quad (11)$$

Here H is the density scale height, ~ 7 km below $z \sim 110$ km, and z subscripts denote derivatives. Figure 2f shows $m^2(z)$ for MWs with $c = 0, l = 0$, for $\lambda_x = 30, 50$, and 80 km. These profiles indicate expected strong influences of the mean environment on MW vertical propagation. While linear theory predicts reflection (negative m^2) for all three wavelengths at several locations within the altitude range 40–105 km, we nonetheless observe waves at these scales aloft prior to wave breaking. At the same time there is a visible filtering of solution components with $\lambda_h < 30$ km above an altitude of ~ 50 km. Thus it appears that linear theory provides only a rough guide regarding reflection for the present case with its highly variable background environment. The m^2 plot also shows the anticipated critical level behavior at altitudes of 85 and 115 km. The value of m^2 is predicted to be large but finite at $z = 85$ km (where $U_h \sim 10 \text{ m s}^{-1}$) and infinite at $z = 115$ km (where $U_h = 0$). As shown in section 3, the wave field responds to the critical levels as expected as these become barriers to wave propagation at early times and as well as sites for instability and turbulence at later times.

f. Subgrid-scale turbulence model

While our 500 m grid spacing is sufficient to resolve both the dominant GW instability structures and the large-scale inertial range turbulent structures it is insufficient to resolve the smaller-scale, mainly dissipative turbulent motions. We account for this reality by incorporating the dynamic Smagorinsky subgrid-scale model (Germano et al. 1991; Moin et al. 1991) in order to mimic the energy drain due to the unresolved turbulent motions. The equations for the eddy viscosity, eddy conductivity, and turbulent kinetic energy coefficients are averaged over limited horizontal planes ($x = [-200: 400]$, $y = [-600, 600]$ km) that contain just the turbulent flow. This is standard treatment and results in well conditioned equations for the model coefficients. The dynamic subgrid-scale model is self-calibrating and thus will only result in enhanced dissipation in actively turbulent regions. Thus the model does not interfere with molecular dissipation that occurs in the largely nonturbulent region above 140 km.

3. Mountain wave evolutions and dynamics

a. Mountain wave and secondary wave evolution in the (x, z) plane at y = −120 km

We begin with an overview of the major features of the MW and secondary wave evolution from $t = 7.5$ to 12 h, where the lower altitude winds increase from 82% to 100% of their maximum values (see Fig. 2c). Figures 3–6 show streamwise-vertical cross sections of $u(x, z)$, $w(x, z)$, $T'/T_0(x, z)$, and spanwise vorticity $\zeta_y(x, z)$, respectively, over the southern peak ($y = -120$ km, hereafter S Peak) at 7.5, 8, 8.5, 9, 10, and 12 h. Movies of the evolutions of these fields, others over N Peak at $y = 120$ km, and in (x, y) planes over both peaks are included for reference in the accompanying support materials.

The earliest responses at 7.5 h extend from lower altitudes into the MLT. Wave reflection, identified by opposite phase slope, is visible below ~ 40 km and downstream of $x = 60$ km (see the u, T'/T_0, and ζ_y fields). Evidence of the anticipated nonhydrostatic behavior in the strong U_0 from ~ 30 to 80 km for $\lambda_x \sim 30$ km is seen most clearly in w. At higher altitudes, very weak MWs are seen in the temperature and vorticity fields at altitudes close to the MW critical level at ~ 115 km. This fact indicates that the near critical level ($U_0 \sim 10 \text{ m s}^{-1}$) at ~ 85 km does not act as a barrier for all wave scales. It does, however, locally compress the vertical wave scale and locally increase the wave amplitude to the extent that it becomes the site for the primary instability.

Increasing cross-mountain flow and especially the rapid nonhydrostatic MW vertical propagation result in much stronger MW and secondary wave responses at 8 h. Strong MW responses and associated instabilities accompanying breaking now extend from the Andes to ~ 150 km eastward. The dominant MW scale has increased to $\lambda_x \sim 50$–60 km, and there are now two strong breaking regions. Initial instabilities arise in the upward and westward phases of the MW, initiate vortex dynamics comprising a succession of vortices having large, negative ζ_y along the MW phase below having negative ζ_y, opposite maxima above and westward, that decouple from the unstable MW phase and are swept downstream (to the east) thereafter while undergoing vortex dynamics driving a rapid cascade to smaller turbulence scales. They now extend from below 60 to above 90 km, and their scales decrease with increasing altitude due to decreasing MW λ_z in decreasing $|c - U_0|$ approaching the U_0 minimum at ~ 85 km.

Additionally, there is now evidence for initial SGW and AW excitation in the MW breaking regions. SGWs having amplitudes of $T'/T_0 \sim 0.1$–0.3 are seen extending more than 100 km upstream of the Andes and to altitudes well above 120 km (see the T'/T_0 and ζ_y fields). Initial, roughly spherical AWs are also seen above the stronger instabilities from $x \sim 40$–150 km. These are most conspicuous in w, but are also seen in u and T'/T_0. They exhibit rapid transitions from warm, rising phases to cooler, descending phases with increasing altitude and have w as large as ~ 50–100 m s^{-1} at this stage of the evolution. The positive correlation of w and T'/T_0 for the AWs is distinct from the quadrature relations anticipated, and seen, for MWs and SGWs.

The MW field and its associated instabilities, SGWs, and AWs continue to intensify to 8.5 and 9 h as cross-mountain winds achieve 95% of their final magnitudes. Stronger forcing is seen to yield a further increase in the dominant MW scale to $\lambda_x \sim 70$ km, an upstream extension over the Andes at ~ 80–115 km including initial instabilities at $z \sim 80$ and 100 km, and instabilities and turbulence extending further downstream with increasing time at altitudes ~ 50–80 km.
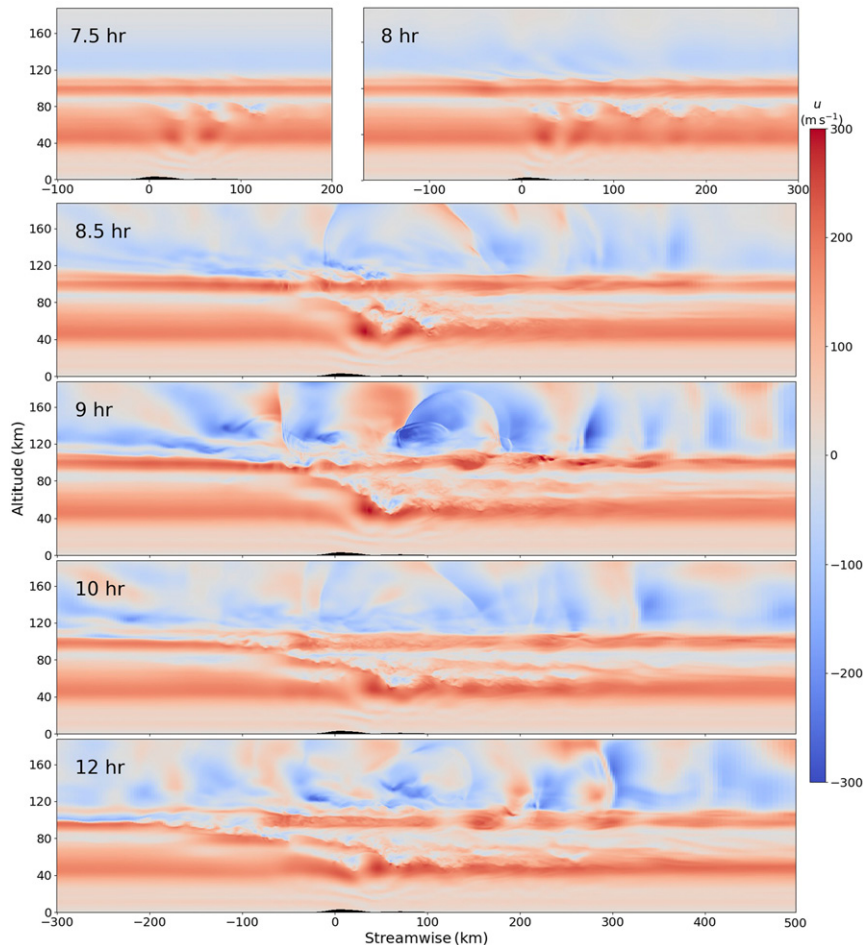
FIG. 3. Cross sections of u (x, z) over the south peak from $z = 0$–180 km and 7.5–12 h (note the expanding streamwise domain at the earlier times).

SGWs increase in amplitude and propagate to the highest altitudes and far upstream and downstream in some cases at these times. Those propagating westward have $\lambda_x \sim 70$–150 km and phase speeds of ~ 80–200 m s^{-1}. The slower of these approach critical levels where $|c - U|$ and λ_z decrease with increasing altitude below ~ 130 km and undergo instabilities and dissipation where $|u'| \sim |c - U| = N\lambda_z/(2\pi)$. Those having larger negative c outrun the westward tidal wind peak at ~ 130 km and refract to larger λ_z where $|c - U|$ increases at higher altitudes. SGWs are also seen propagating eastward, but these have very different character because of the large-scale U and T fields. The primary eastward-propagating SGW at these times has $\lambda_x \sim 65$ km and $c \sim 220$ m s^{-1}, and exhibits ducting at ~ 90–110 km, an increasing amplitude in time, evolving instabilities accompanying the eastward u' maxima and ζ_y minima, and additional laminar maxima that are in quadrature due to evanescence above ~ 120 km [see the movies of this evolution in the (x, z) plane in the accompanying materials]. The features enabling these eastward-propagating ducted SGWs are the m^2 maxima seen for the gray line (for $\lambda_x = 65$ km and $c = 220$ m s^{-1}) in Fig. 2f at ~ 105 and 110 km. This m^2 maximum,

and the negative m^2 above and below, comprise a duct that occurs due to $-U_{zz}/U > 0$ at ~ 100 km and large N^2/U^2 at ~ 108 km; see the first two terms on the right-hand side of Eq. (11).

AWs likewise become much stronger by 9 h and arise at ~ 2–3 min intervals in the strong MW breaking regions at lower altitudes. These have phase speeds $c_{AW} \sim 500$ m s^{-1} at higher altitudes, velocities normal to their phase surfaces, and continue to exhibit roughly spherical phase fronts suggesting very localized sources. Their phase fronts are not strictly spherical because $T(z)$ and $c_{AW} \sim T^{1/2}$ increase strongly between their source altitudes and ~ 150 km. AW amplitude increases with increasing altitude drive their evolution to shock waves having very sharp transitions from warm rising phases to cold descending phases in many cases. As when first seen, they appear to be strongly correlated with the regions of most intense instability dynamics accompanying MW breaking from ~ 50 to 80 km (see F20).

The subsequent evolution of the MW field is shown at 10 and 12 h in the bottom two panels of Figs. 3–6. These reveal significant reductions in the strength of MW instability dynamics
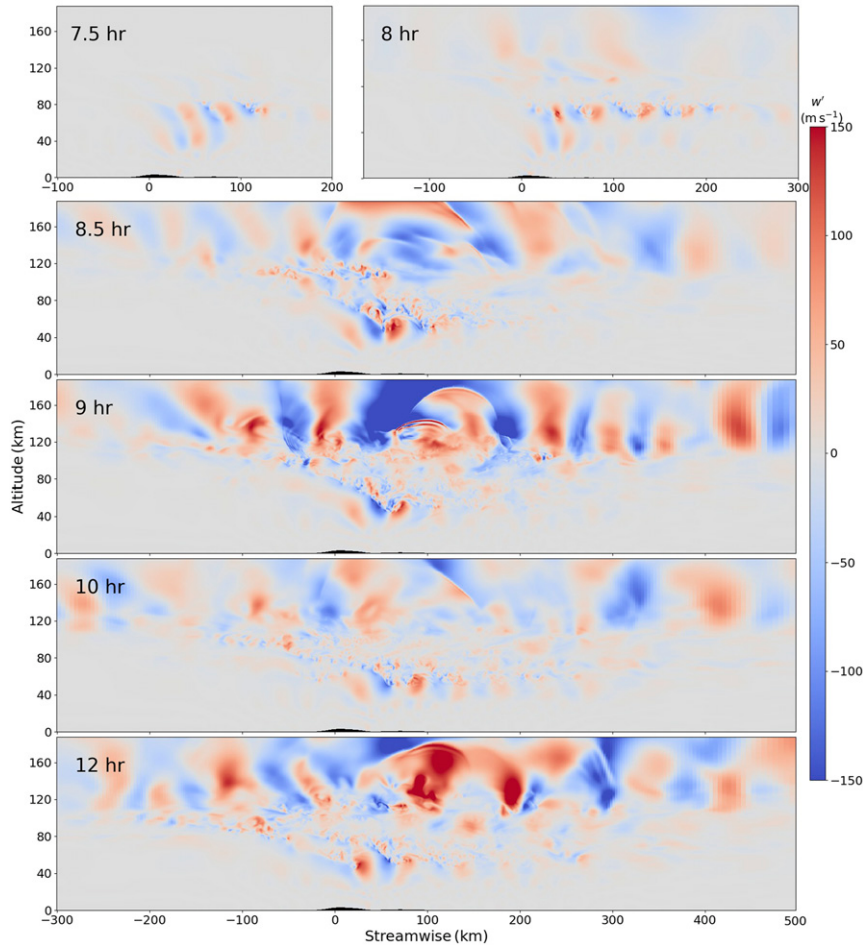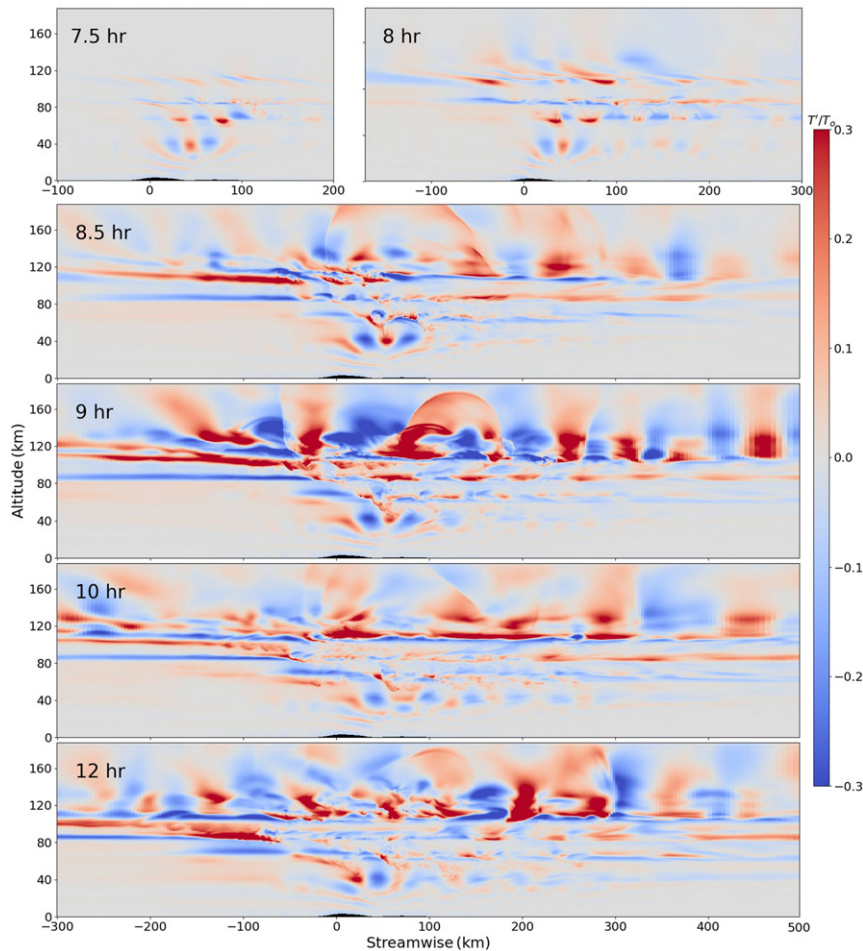
FIG. 4. As in Fig. 3, but for w.

from ~45 to 115 km, of SGW and AW amplitudes above ~85 km, and of SGW instabilities in the lee of the Andes that were prominent at 9 h. This is despite the cross-mountain flow reaching its peak amplitude during this interval. Also seen at 10 and 12 h is a continuation of the increase in the dominant MW scale λ_x over and upstream of the Andes. Stationary MWs have $\lambda_x \sim$ 150–200 km at $z \sim$ 75 km over and ~200 km upstream of the Andes at 10 h, and this shifts to somewhat larger λ_x, higher altitudes, and further upstream by 12 h, revealing increasing relative roles for the larger MW λ_x seen in the terrain k spectral power in Fig. 1c at later times.

We now explore the apparent causes for decreasing smaller-λ_x MWs and their associated SGW, AW, and instability responses over S Peak after 9 h. Shown at left in Fig. 7 are cross sections of ζ_y in a subdomain at $x = 0$–100 km and $z = 0$–30 km from 7.5 to 12 h (see dashed box at 9 h in Fig. 6). MW forcing has achieved ~70% of its peak amplitude by 7 h, and the MW amplitude in the lower stratosphere has achieved ~70% of its peak amplitude by ~7.5 h, based on the scales seen in Fig. 2 and inferred c_{gz}. Dominant MW responses are seen at $\lambda_x \sim$ 50–80 km over and in the lee of S Peak. However, there are also transient responses

apparently arising from temporally variable flow over the mountain peak. These appear to contribute to modulation of the MWs and to other GWs propagating upward to the E up to ~9 h.

The MWs at $x \sim$ 0–60 km exhibit instabilities beginning prior to 8 h and extending throughout this interval. Specifically, strong, small-scale vorticity dynamics begin prior to 8 h, modulate the MW amplitude at ~20 km initially, then more aggressively and extending to lower altitudes at ~10 h and thereafter. Characteristic scales of these instability dynamics are ~3–4 km, consistent with expectations for $\lambda_z \sim$ 10–15 km and strong breaking (Fritts et al. 2009), and they necessarily reduce MW amplitudes at higher altitudes thereafter. These dynamics have the same character and scales seen over S Peak from ~80 and 100 km at 8.5 and 9 h in Fig. 6, where U and the MW λ_z are comparable to those in the lower stratosphere. They are also similar to the instabilities from ~50 to 70 km from 8 to 9 h, where the MW instability scales are larger due to larger $\lambda_z > 2\pi U/N$, and which strongly reduce MW amplitudes due to breaking. MW instability dynamics, momentum fluxes, tidal interactions, and their influences are examined in greater detail by F19b and F20.

FIG. 5. As in Fig. 3, but for T'/T_0.

b. Comparison of MW and secondary wave evolutions over and around S Peak and N Peak

The N and S Peak have roughly linear N–S Peak terrain extending ~60 and 150 km, respectively, but very different east–west terrain. To compare the responses to the different terrain, and explore the broader responses to the southern Andes massifs, we show $u(x, z)$ cross sections over N Peak from 7.5 to 9 h in the upper panels of Fig. 8 for comparison with those over S Peak at these times in Fig. 3, with the (x, z) cross sections at $y = \pm120$ km; Fig. 7 shows $\zeta_y(x, z)$ cross sections over N Peak from 7.5 to 12 h at right for comparison with those over S Peak at left; Fig. 9 provides more extended (y, z) cross sections of u', v', w', and T'/T_0 at $x = 50$ km and 9 h; finally, Figs. 10–12 show (x, y) cross sections of u, w' and T'/T_0, respectively, at 8, 9, and 10 h (left to right) at altitudes of 70, 100, 120, and 180 km (top to bottom).

As seen in $u(x, z)$ over S Peak (Fig. 3), N Peak (Fig. 8, top panels) yields emerging MW breaking downstream and generation of SGWs and AWs having similar scales and character that readily propagate to higher altitudes. Compared to S Peak, however, N Peak exhibits weaker lee MW overturning, less

significant trailing turbulence from ~40 to 100 km, much less upstream MW penetration above ~70 km, and weaker SGW and AW responses everywhere. The cross sections at $y = \pm120$ km do not provide a complete picture, however, because the responses include expanding strong MW breaking, turbulence, and their consequences much further N and S along the southern Andes at later times. The $u'(y, z)$ cross sections at the bottom in Fig. 8 show the breaking regions in the lee of each massif to dip below $z = 50$ km at $x = 50$ km, and to extend significantly N and S at $z \sim 60$–80 and ~100 km at 9 and 10 h, with the strongest instability dynamics where u' is most negative. Alternating bands of $u' > 0$ and <0 at adjacent altitudes reveal the local MW λ_z, its variations in altitude with varying $U(z)$, and the modulation of the MW phase along y. The downward extensions indicate where MW breaking is nearer the spine of the Andes because of the upward and westward MW phase slopes, suggesting that MWs having smaller λ_x contribute preferentially to stronger breaking (also see Figs. 10–12 below).

A broader perspective of the responses to strong MW forcing over the southern Andes is provided in the perturbation fields in Fig. 9 showing (y, z) cross sections extending
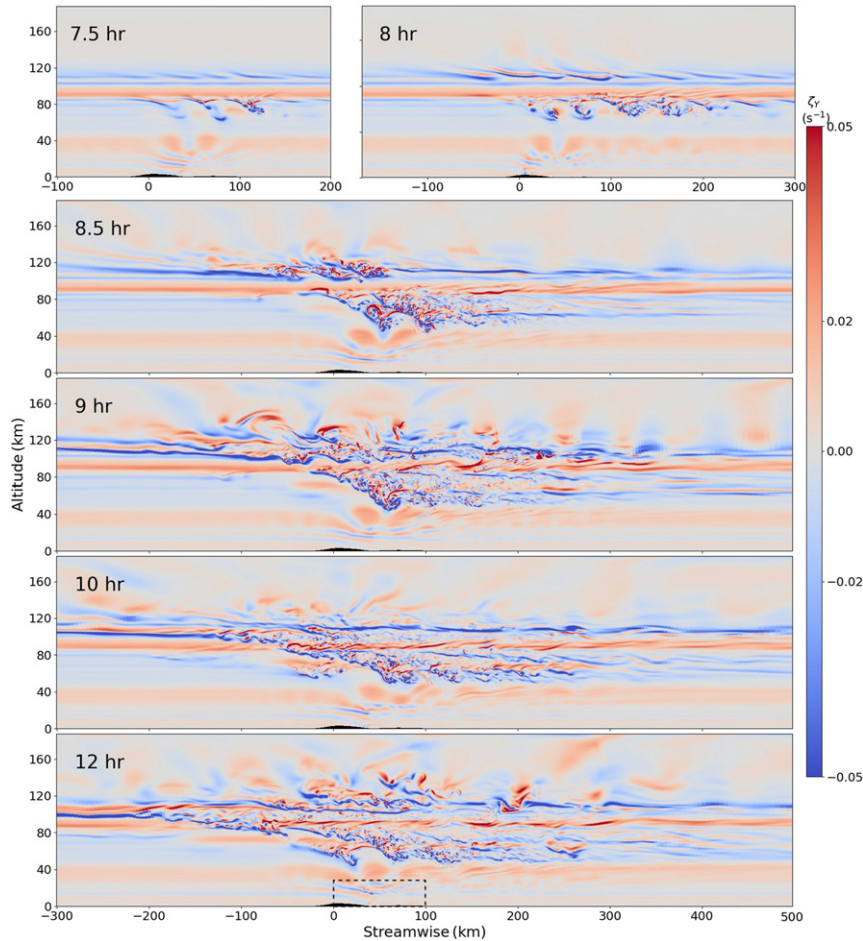
FIG. 6. As in Fig. 3, but for ζ_y. (bottom) The dashed box shows the region depicted in Fig. 7.

1800 km in y and in Figs. 10–12 showing horizontal cross sections spanning 1200–1800 km in x and y at $z = 70$, 100, 120, and 180 km. Considering first the u', w', and T'/T_0 fields in Fig. 9 and at 70 km in Figs. 10–12, we see that strong MW responses and breaking occur over the highest terrain at $|y| < 300$ km (Figs. 9–12 at top), but that strong flow over lower terrain yields significant MWs extending to $|y| > 500$ km at 9 h. Strong MW breaking also expands E–W and to higher altitudes at 9 and 10 h (approaching the MW critical level at $z \sim 114$ km, as seen above). These fields, especially the v' and $T'/T_0(y, z)$ cross sections and the (x, y) cross sections, reveal SGWs and AWs extending to ~120–180 km and laterally to the edges of the computational domain.

The plots of $u'(y, z)$ in Fig. 10 at 8 h exhibits large MW amplitudes and strong zonal decelerations at 70 km that are localized in y in the lee of N Peak and S Peak, but extend multiple MW λ_x (~200 km) downstream. Similar responses are seen at 100 km, but with MW propagation toward N of W due to influences of $V < 0$ below, which favors propagation in the direction of largest $c_i = (c - U_h)$. Specifically, these reveal $|u'|$ exceeding $|c - U|$ in the evolving local mean wind, $U(x, y, z, t)$, where c may acquire westward values (e.g., westward self

acceleration) due to local $dU/dt < 0$ accompanying MW momentum deposition. This is confirmed by $|T'/T_0|$ exceeding an overturning threshold for the relevant λ_z. These dynamics advance the MW phases westward at the locations of strongest $dU/dt < 0$, as seen in Fig. 10 at 70 and 100 km at 8 h.

Varying $dU(x, y, z)/dt$ due to MW momentum deposition contributes advection of the MW phases (e.g., self acceleration) that varies with MW amplitude along the MW phase, compresses the MW λ_x upstream of the strongest dU/dt, and accounts for the phase variations seen in the lower panels of Fig. 8 and the smaller (larger) λ_x at the upstream (downstream) edges of the regions of strongest breaking. These dynamics account for the "ship wave" patterns centered over each peak and having MW phases to the N and S of each further downstream at 8 h, implying outward (partial N–S) MW propagation from localized sources at lower altitudes. Strong zonal decelerations apparent over N Peak and S Peak at 8 h and 70 km are seen to have compensating (eastward) $U(x, y)$ accelerations between, and N and S of, N Peak and S Peak, to satisfy continuity in the larger-scale flow. The local decelerations seen at 8 h and 70 km are seen to merge in latitude at later times as the large-scale mean flow, $(U, V, W)(x, y, z, t)$, adjusts to the
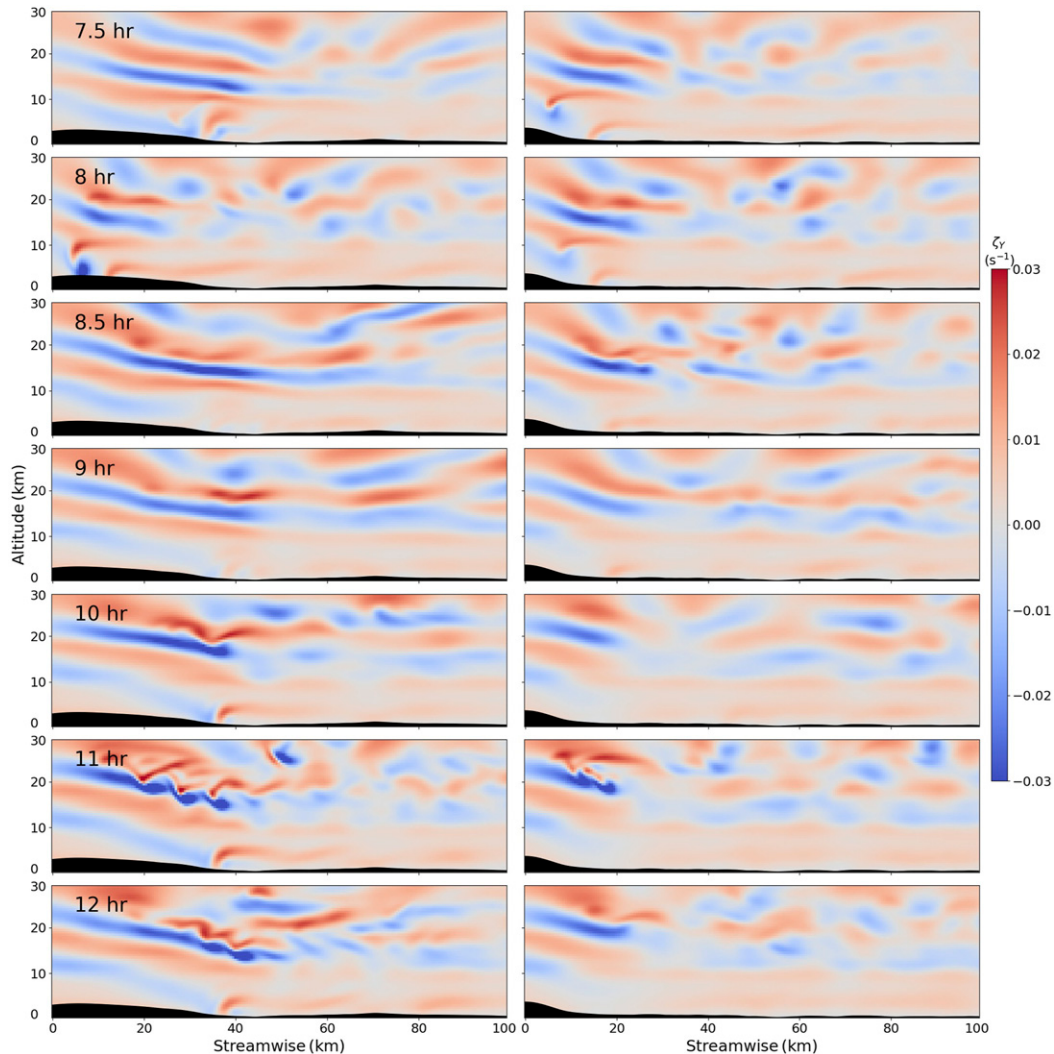
FIG. 7. As in Fig. 3, but for ζ_y in subdomains covering $x = 0$–100 km and $z = 0$–30 km at 30-min intervals from 9 to 12 h over the (left) south peak and (right) north peak.

localized and variable 3D MW momentum deposition in space and time. This causes an evolution to a larger ship-wave response over both peaks, weaker at 70 km and much stronger at 100 km, seen in Figs. 10–12 at 9 and 10 h.

The (x, y) cross sections also reveal more clearly the emerging SGW scales, typically $\lambda_x \sim 200$ km and larger, and roughly circular, outward phase propagation beginning at $z \sim 100$ km and extending with increasing scales and amplitudes to higher altitudes. Additionally, (x, y) cross sections from 100 to 180 km, especially w' and T'/T_0 at smaller radii, reveal nearly circular features beginning to emerge at 8 h that intensify with altitude and time to 9 h, but have large amplitudes and gradients only within ~ 200 km of the regions of strong MW breaking at lower altitudes. These are the AWs seen in the vertical cross sections above, and are clearly stronger over the more intense MW breaking over S Peak. See especially Figs. 11 and 12 at 8 and 9 h.

SGW and AW responses at 10 h in Figs. 3–5 and 10–12 exhibit significantly reduced amplitudes compared to those at 9 h

over N Peak and S Peak, despite continuing increases in MW forcing at the lowest altitudes. MW, and associated SGW and AW, amplitude reductions over S Peak after 9 h are attributed above to emerging MW breaking below 30 km over S Peak, and associated decreasing small-λ_x amplitudes extending to higher altitudes as a result of the approach to the strongest cross-mountain flow at low altitudes. We see, for example, that MWs having small λ_x and large ω_i, hence large c_{gz}, exhibit somewhat weaker amplitudes and instabilities at 70 and 100 km at 10 h. This is because influences of decreasing forcing for these MWs due to instabilities at ~ 30 km and below are quickly communicated to higher altitudes. The most rapid reductions of SGW amplitudes above ~ 100 km accompany smaller λ_h, hence larger ω_i and c_{gz}, enabling them to propagate most quickly to higher altitudes. By comparison, SGWs excited by larger-scale MWs and having larger λ_h, hence smaller ω_i and c_{gz}, are seen to persist to 10 h at 120 and 180 km at greater distances from their sources (see especially
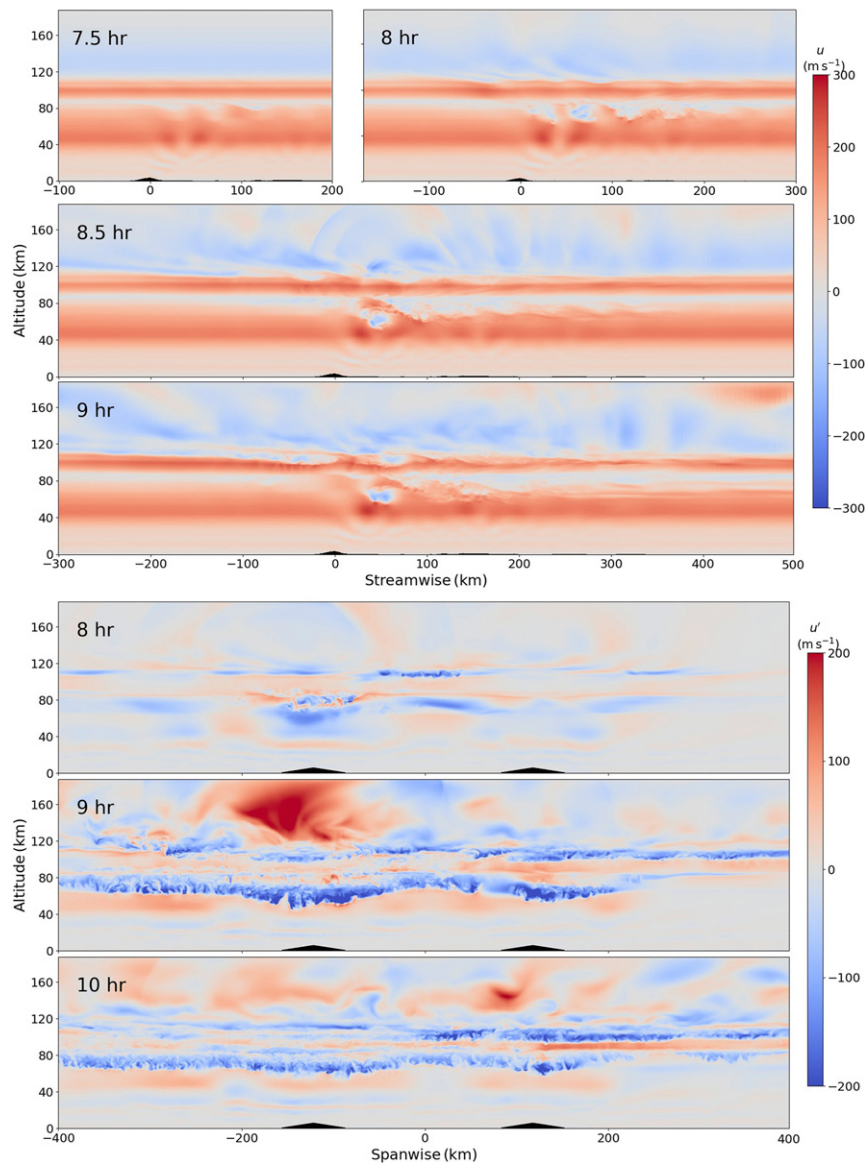
FIG. 8. Contours of u and u' over the north peak at the times indicated. The top three rows are streamwise–vertical views of u, whereas the bottom three are spanwise–vertical views of u' at $x = 50$ km. The black triangles near the ground in the latter are approximations to the mountain peaks, projected onto the downstream view.

Figs. 10 and 12), and even exhibit increasing amplitudes again by 12 h (see Figs. 3–5).

In contrast, MWs having $\lambda_h \sim 200$–300 km propagate vertically much more slowly, requiring multiple hours to penetrate the weak zonal winds in the troposphere, lower stratosphere, and near 85 km. Hence the $\lambda_x \sim 150$–300 km MWs excited prior to 9 h continue to propagate upward, grow in amplitude with altitude, exhibit increasing responses to ~10 h and beyond, and excite SGWs arising from these dynamics in the stratosphere and MLT that persist to 10–12 h. As examples, see the larger MW amplitudes and accompanying instabilities at ~50–115 km in Figs. 3–6 at

10 and 12 h and the larger-scale MW instabilities at 100 km at 10 h in Figs. 10 and 12.

As noted in the discussion of the ζ_y fields over S Peak, unsteady flow occurs over N Peak prior to ~7.5 h, but subsides by 10 h (see Fig. 7 at right). MW instabilities also occur over N Peak and impact MW amplitudes prior to 9 h, again after 10 h, and perhaps between at nearby latitudes. These dynamics appear to have somewhat lesser roles over N Peak compared to S Peak, as suggested by the SGW and AW responses at higher altitudes discussed above. However, they do not prevent similar MW and instability features over both peaks and extending over significant distances N and S spanning multiple hours.
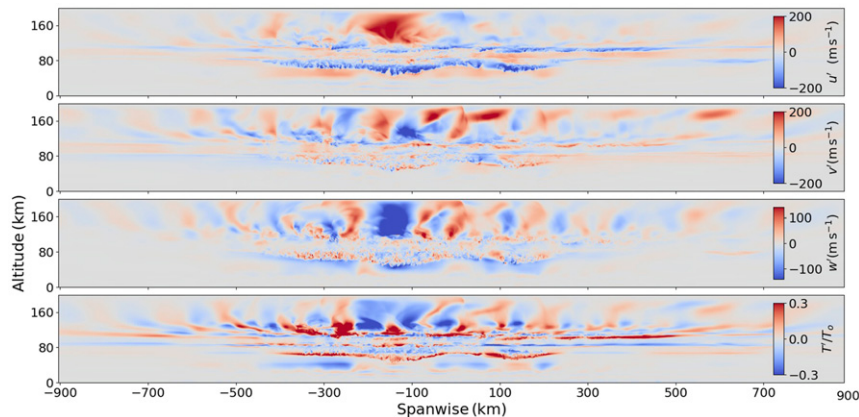
FIG. 9. (y, z) cross sections of u', v', w', and T'/T_0 at $x = 50$ km and 9 h.

c. Impacts of MW dynamics and momentum transport and deposition on large-scale winds

Induced mean wind changes accompanying strong MW breaking were noted in the discussion of the $u'(x, y)$ fields at 70 km in Fig. 10. Evidence of such changes are also seen in Fig. 3 beginning at 8.5 h and increasing to later times. These were not discussed above because stationary MWs having large λ_x can yield varying $u(x, z)$ that could be confused with mean wind variations due to local momentum deposition. With the knowledge that $U(z = 70 \text{ km})$ varies in x and y, we can return to Fig. 3 to explore variations in z as well. The $u'(x, y)$ field in Fig. 10 at 70 km and 8 h reveals strong, eastward U deficits localized over N and S Peaks. Responses at 70 km have weakened, merged along y, and extended >500 km downstream by 9 h. By 10 h, they have further expanded downstream, significantly northward, somewhat southward, and another ~100 km westward. Compensating U enhancements in all of these fields occur between and/or at the edges of the U deficits at these times.

Similar responses are also seen at 100 km in Fig. 10, but with interesting differences. As this altitude is above the primary wave breaking zone, we are observing a combination of primary and secondary waves, with the later becoming dominant as time progresses. Larger-λ_h MWs play a larger role at 100 km. At 8 h, they extend ~200 km farther upstream and have distinct ship-wave responses over N and S Peaks oriented somewhat N of W. This pattern evolves to a larger ship-wave response to an apparent single, larger obstacle at lower altitudes from 8 to 10 h, imposes a U deficit spanning a significantly larger area than at 70 km, and is likewise oriented slightly N of W. The response also now exhibits a U deceleration (acceleration) at the N (S) center that exhibits a bias in y that is opposite to that seen at 70 km at 9 and 10 h.

The rotation of the response at 100 km can be traced to the contribution of the meridional wind to favorable MW penetration to higher altitudes, but having a WNW orientation, as noted above. Referring to Fig. 2b, we see that MWs oriented somewhat N of W have a larger headwind below 100 km than those oriented S of W. This favors attainment of larger MW amplitudes inclined N of W seen at 8 h, and

implies larger $|c - U_h|$ and stronger decelerations at and below 100 km to the N of the response center at 9 and 10 h by these MWs. Those oriented S of W to the S of the response center encounter decreasing headwinds, smaller $|c - U_h|$, experience stronger amplitude constraints, and impose weaker forcing, consistent with the observed U deficits or enhancements at 9 and 10 h.

Referring to Figs. 3 and 8, we see that there are significant U deficits in the lee of N and S Peaks beginning at 70 km and expanding up to ~80 and down to ~50 km from 8 to 10 h that span several MW cycles and are thus not due to a larger-scale MW. In the same manner, the $u'(x, y)$ fields at 100 km in Fig. 10 reveal a lack of a significant U deficit in the lee of S Peak and a weaker deficit associated largely with a larger-λ_x MW imposing $u' < 0$ extending farther upstream at later times, which are consistent with inferences from the (x, y) fields discussed above.

4. Discussion

We have presented the first large-scale compressible simulation of MW dynamics arising from increasing near-surface winds blowing over realistic high terrain. High resolution in the central domain enabled realistic descriptions of initial instability dynamics and realistic MW dissipation, momentum deposition, and secondary wave generation extending into the MLT. A slow ramp of the cross-mountain flow avoided nonphysical transients, revealed the initial occurrence of MW breaking and instability dynamics in the mesosphere under linear MW propagation conditions at lower altitudes, and demonstrated the weakening of MLT responses following MW breaking at lower altitudes. Responses in the MLT included 1) instability and wave breaking at the near critical level at $z = 85$ km (where $U_h \sim 10 \text{ m s}^{-1}$) 2) generation of SGWs able to propagate to higher altitudes and upstream, downstream, and laterally from the forcing terrain, 3) generation of AWs able to achieve shock wave character in the MLT and penetrate quickly to higher altitudes, and 4) large-scale ship-wave responses and local flow decelerations extending into the thermosphere.

Our results validate the initial studies by Schoeberl (1985) and Bacmeister (1993) suggesting MW influences extending
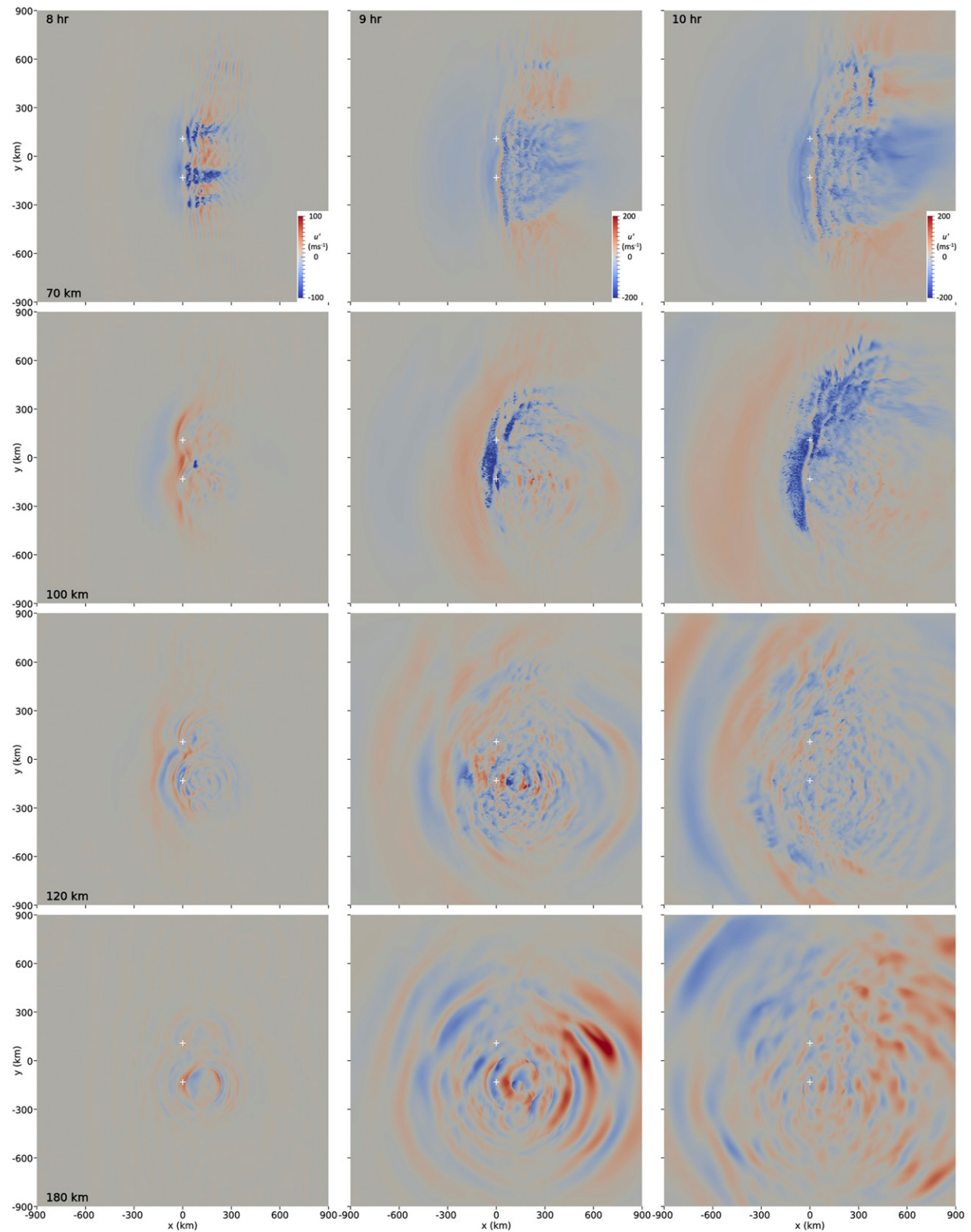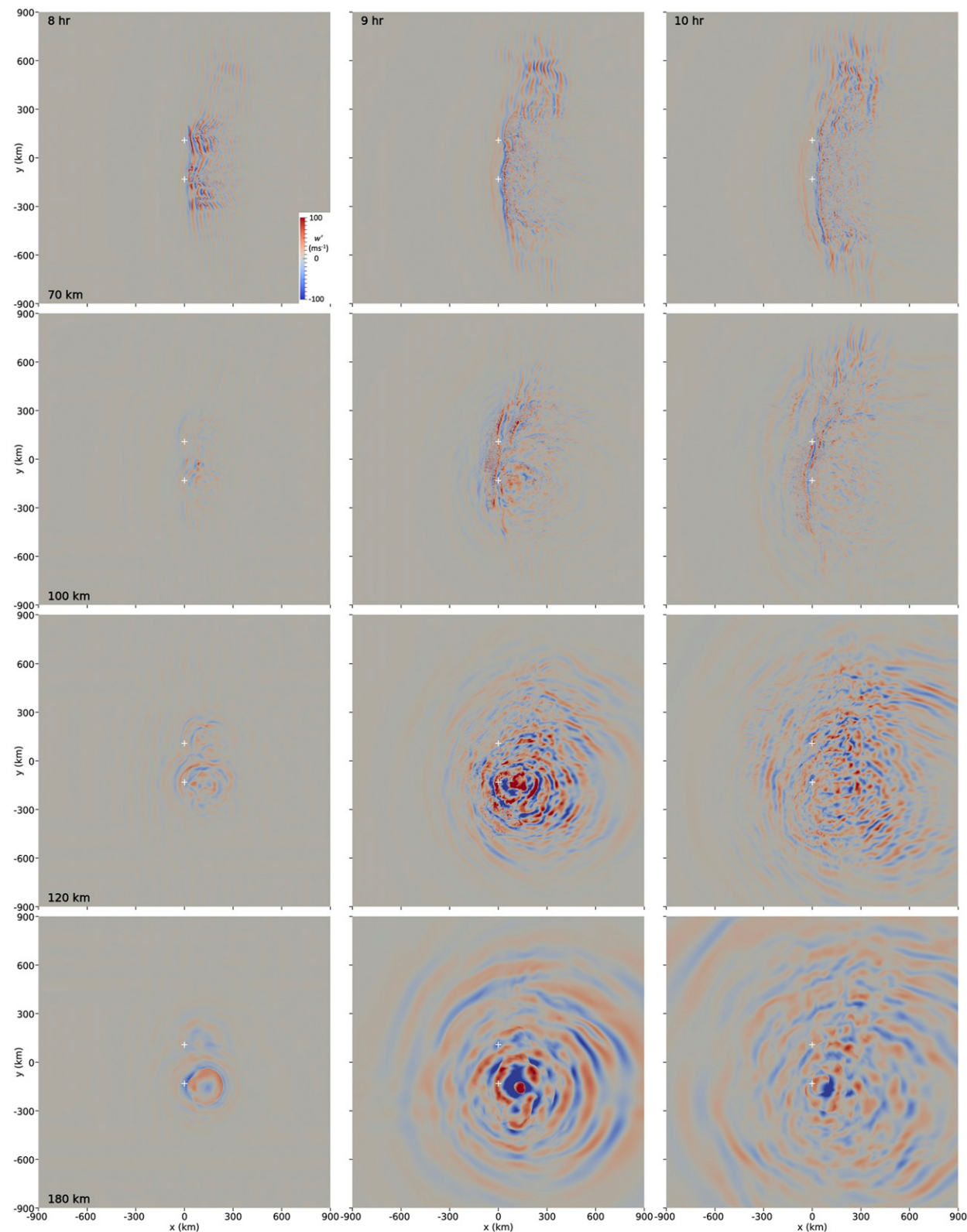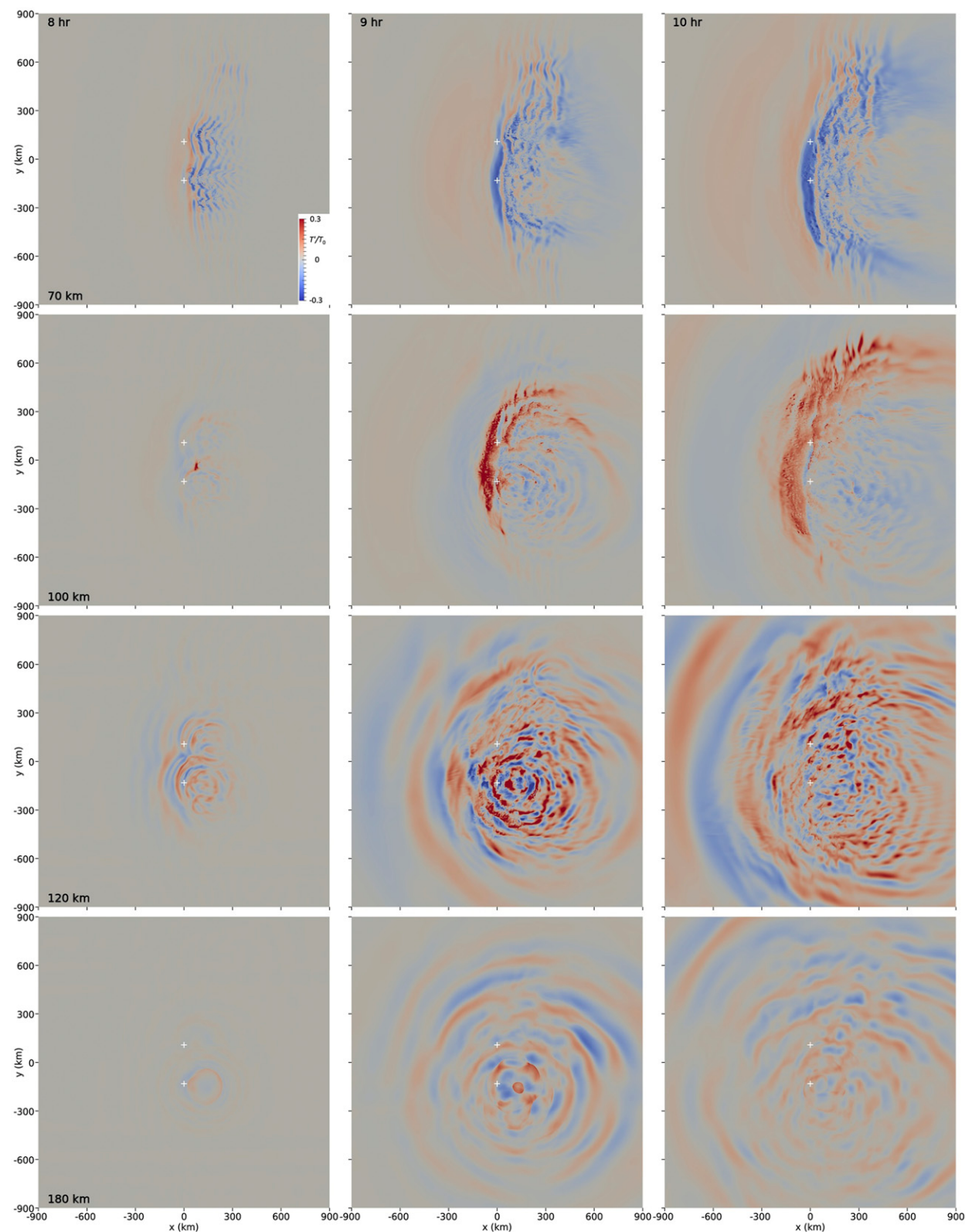
FIG. 10. (top to bottom) Cross sections of $u'(x, y)$ at 70, 100, 120, and 180 km and (left to right) times of 8, 9, and 10. The positions of the north and south peaks are shown with plus signs.

FIG. 11. As in Fig. 10, but for w'.

FIG. 12. As in Fig. 10, but for T'/T_0.

into the MLT. They confirm the potential noted in previous studies for smaller- and larger-scale MWs to penetrate into the MLT and exhibit strong breaking and/or SGW generation over the Andes (Smith et al. 2009; de Wit et al. 2017; Becker and Vadas 2018; Hecht et al. 2018) and New Zealand (Smith et al. 2013; Bossert et al. 2015, 2017, 2018; Kaifler et al. 2015; Eckermann et al. 2016; Fritts et al. 2016, 2018; Pautet et al. 2016; Bramberger et al. 2017; Broutman et al. 2017). They also suggest the potential for such responses to accompany MW generation over other large- and small-scale terrain at middle and high latitudes and to extend well into the thermosphere under suitable propagation conditions. Other implications of this simulation addressing MW and SGW momentum deposition, mean forcing, tidal interactions, and instability dynamics in the lower atmosphere and MLT are discussed in the companion papers F19a and F19b.

5. Conclusions

Our results demonstrate the complex interworking of GW generation, propagation, refraction, and instability accompanying MW dynamics. Furthermore, we have shown that wave breaking and the attendant momentum deposition provides sources for both SGWs and AWs that propagate freely into the lower thermosphere. Since the secondary waves have nonzero ground-based frequency, they are unaffected by the MW critical level at 115 km. The secondary waves carry sufficient momentum and energy to measurably alter the mean state as they are ultimately dissipated at altitudes above our model top.

It should be noted that nearly all of these complicated physical processes cannot be described with linear theory. We have shown that even refraction of the primary waves is not well predicted by the theory, presumably due to a failure of the WKB approximation required to account for the highly variable background environments. This situation provides a challenge for GW parameterization schemes required in low- to medium-resolution numerical models. Simple saturation schemes would predict that all of the primary wave momentum is deposited at the critical level at 115 km and a more sophisticated ray tracing approach would predict that most of the wave energy is reflected at lower levels. Our numerical simulation database provides a unique tool for constructing improved parameterizations and we are currently working on producing such a product.

REFERENCES

Bacmeister, J. T., 1993: Mountain-wave drag in the stratosphere and mesosphere inferred from observed winds and a simple mountain-wave parameterization scheme. *J. Atmos. Sci.*, **50**, 377–399, https://doi.org/10.1175/1520-0469(1993)050<0377:MWDITS>2.0.CO;2.

Becker, E., and S. L. Vadas, 2018: Secondary gravity waves in the winter mesosphere: Results from a high-resolution global circulation model. *Geophys. Res. Lett.*, **123**, 2605–2627, https://doi.org/10.1002/2017JD027460.

Bossert, K., and Coauthors, 2015: Momentum flux estimates accompanying multiscale gravity waves over Mount Cook, New Zealand, on 13 July 2014 during the DEEPWAVE campaign. *J. Geophys. Res. Atmos.*, **120**, 9323–9337, https://doi.org/10.1002/2015JD023197.

——, C. G. Kruse, C. J. Heale, D. C. Fritts, B. P. Williams, J. B. Snively, P.-D. Pautet, and M. J. Taylor, 2017: Secondary gravity wave generation over New Zealand during the DEEPWAVE campaign. *J. Geophys. Res. Atmos.*, **122**, 7834–7850, https://doi.org/10.1002/2016JD026079.

——, and Coauthors, 2018: Momentum flux spectra of a mountain wave event over New Zealand. *J. Geophys. Res. Atmos.*, **123**, 9980–9991, https://doi.org/10.1029/2018JD028319.

Bramberger, M., and Coauthors, 2017: Does strong tropospheric forcing cause large-amplitude mesospheric gravity waves? A DEEPWAVE case study. *J. Geophys. Res. Atmos.*, **122**, 11 422–11 443, https://doi.org/10.1002/2017JD027371.

Broutman, D., S. D. Eckermann, H. Knight, and J. Ma, 2017: A stationary phase solution for mountain waves with application to mesospheric mountain waves generated by Auckland Island. *J. Geophys. Res. Atmos.*, **122**, 699–711, https://doi.org/10.1002/2016JD025699.

Coppola, G., F. Capuano, S. Pirozzoli, and L. de Luca, 2019: Numerically stable formulations of convective terms for turbulent compressible flows. *J. Comput. Phys.*, **382**, 86–104, https://doi.org/10.1016/j.jcp.2019.01.007.

de Wit, R. J., D. Janches, D. C. Fritts, R. G. Stockwell, and L. Coy, 2017: Unexpected climatological behavior of MLT gravity wave momentum flux in the lee of the southern Andes hot spot. *Geophys. Res. Lett.*, **44**, 1182–1191, https://doi.org/10.1002/2016GL072311.

Dong, W., D. C. Fritts, T. S. Lund, S. A. Wieland, and S. Zhang, 2019: Self-acceleration and instability of gravity wave packets: 2. Two-dimensional packet propagation, instability dynamics, and transient flow responses. *J. Geophys. Res. Atmos.*, **125**, e2019JD030691, https://doi.org/10.1029/2019JD030691.

Doyle, J. D., M. A. Shapiro, Q. Jiang, and D. L. Bartels, 2005: Large-amplitude mountain waves over Greenland. *J. Atmos. Sci.*, **62**, 3106–3126, https://doi.org/10.1175/JAS3528.1.

Eckermann, S. D., and Coauthors, 2016: Dynamics of orographic gravity waves observed in the mesosphere over the Auckland Islands during the Deep Propagating Gravity Wave Experiment (DEEPWAVE). *J. Atmos. Sci.*, **73**, 3855–3876, https://doi.org/10.1175/JAS-D-16-0059.1.

Felten, F. N., and T. S. Lund, 2006: Kinetic energy conservation issues associated with the collocated mesh scheme for incompressible flow. *J. Comput. Phys.*, **215**, 465–484, https://doi.org/10.1016/j.jcp.2005.11.009.

Fritts, D. C., L. Wang, J. Werne, T. Lund, and K. Wan, 2009: Gravity wave instability dynamics at high Reynolds numbers. Part II: Turbulence evolution, structure, and anisotropy. *J. Atmos. Sci.*, **66**, 1149–1171, https://doi.org/10.1175/2008JAS2727.1.

——, and Coauthors, 2016: The Deep Propagating Gravity Wave Experiment (DEEPWAVE): An airborne and ground-based exploration of gravity wave propagation and effects from their sources throughout the lower and middle atmosphere. *Bull. Amer. Meteor. Soc.*, **97**, 425–453, https://doi.org/10.1175/BAMS-D-14-00269.1.

——, and Coauthors, 2018: Large-amplitude mountain waves in the mesosphere accompanying weak cross-mountain flow during DEEPWAVE research flight RF22. *J. Geophys. Res. Atmos.*, **123**, 9992, https://doi.org/10.1029/2017JD028250.

——, M. J. Taylor, P.-D. Pautet, N. R. Criddle, B. Kaifler, L. Wang, S. D. Eckermann, and B. Liley, 2019a: Large-amplitude mountain waves in the mesosphere observed on 21 June 2014 during DEEPWAVE: 2. Nonlinear dynamics, wave breaking, and instabilities. *J. Geophys. Res.*, **124**, 10 006–10 032, https://doi.org/10.1029/2019JD030899.

Geller, M. A., and Coauthors, 2013: A comparison between gravity wave momentum fluxes in observations and climate models. *J. Climate*, **26**, 6383–6405, https://doi.org/10.1175/JCLI-D-12-00545.1.

Germano, M., U. Piomelli, P. Moin, and W. H. Cabot, 1991: A dynamic subgrid-scale eddy viscosity model. *Phys. Fluids.*, **3**, 1760–1765, https://doi.org/10.1063/1.857955.

Goldberg, R. A., and Coauthors, 2006: The MaCWAVE program to study gravity wave influences on the polar mesosphere. *Ann. Geophys.*, **24**, 1159–1173, https://doi.org/10.5194/angeo-24-1159-2006.

Hastings, D. A., and Coauthors, Eds., 1999: The Global Land One-Kilometer Base Elevation (GLOBE) digital elevation model, version 1.0. NOAA National Geophysical Data Center, accessed 15 September 2017, https://www.ngdc.noaa.gov/mgg/topo/globe.html.

Heale, C. J., K. Bossert, J. B. Snively, D. C. Fritts, P.-D. Pautet, and M. J. Taylor, 2017: Numerical modeling of a multiscale gravity wave event and its airglow signatures over Mount Cook, New Zealand, during the DEEPWAVE campaign. *J. Geophys. Res. Atmos.*, **122**, 846–860, https://doi.org/10.1002/2016JD025700.

Hecht, J. H., and Coauthors, 2018: Observations of the breakdown of mountain waves over the Andes Lidar Observatory at Cerro Pachon on 8/9 July 2012. *J. Geophys. Res. Atmos.*, **123**, 276–299, https://doi.org/10.1002/2017JD027303.

Hendricks, E. A., J. D. Doyle, S. D. Eckermann, Q. Jiang, and P. A. Reinecke, 2014: What is the source of the stratospheric gravity wave belt in austral winter? *J. Atmos. Sci.*, **71**, 1583–1592, https://doi.org/10.1175/JAS-D-13-0332.1.

Hertzog, A., G. Boccara, R. A. Vincent, F. Vial, and P. Cocquerez, 2008: Estimation of gravity wave momentum flux and phase speeds from quasi-Lagrangian stratospheric balloon flights. Part II: Results from the Vorcore campaign in Antarctica. *J. Atmos. Sci.*, **65**, 3056–3070, https://doi.org/10.1175/2008JAS2710.1.

Hou, Y. C., and K. Mahesh, 2005: A robust, colocated, implicit algorithm for direct numerical simulation of compressible, turbulent flows. *J. Comput. Phys.*, **205**, 205–221, https://doi.org/10.1016/j.jcp.2004.10.039.

Jiang, Q., J. D. Doyle, S. Wang, and R. B. Smith, 2007: On boundary layer separation in the lee of mesoscale topography. *J. Atmos. Sci.*, **64**, 401–420, https://doi.org/10.1175/JAS3848.1.

——, ——, S. D. Eckermann, and B. P. Williams, 2019: Stratospheric trailing gravity waves from New Zealand. *J. Atmos. Sci.*, **76**, 1565–1586, https://doi.org/10.1175/JAS-D-18-0290.1.

Kaifler, B., N. Kaifler, B. Ehard, A. Dörnbrack, M. Rapp, and D. C. Fritts, 2015: Influences of source conditions on mountain wave penetration into the stratosphere and mesosphere. *Geophys. Res. Lett.*, **42**, 9488–9494, https://doi.org/10.1002/2015GL066465.

Kim, Y.-J., S. D. Eckermann, and H.-Y. Chun, 2003: An overview of the past, present and future gravity-wave drag parametrization for numerical climate and weather prediction models. *Atmos.–Ocean*, **41**, 65–98, https://doi.org/10.3137/ao.410105.

Kruse, C. G., R. B. Smith, and S. D. Eckermann, 2016: The mid-latitude lower-stratospheric mountain wave "valve layer." *J. Atmos. Sci.*, **73**, 5081–5100, https://doi.org/10.1175/JAS-D-16-0173.1.

Leutbecher, M., and H. Volkert, 2000: The propagation of mountain waves into the stratosphere: Quantitative evaluation of three-dimensional simulations. *J. Atmos. Sci.*, **57**, 3090–3108, https://doi.org/10.1175/1520-0469(2000)057<3090:TPOMWI>2.0.CO;2.

Liu, H.-L., 2016: Variability and predictability of the space environment as related to lower atmosphere forcing. *Space Wea.*, **14**, 634–658, https://doi.org/10.1002/2016SW001450.

——, J. M. McInerney, S. Santos, P. H. Lauritzen, M. A. Taylor, and N. M. Pedatella, 2014: Gravity waves simulated by high-resolution Whole Atmosphere Community Climate Model. *Geophys. Res. Lett.*, **41**, 9106–9112, https://doi.org/10.1002/2014GL062468.

Lott, F., 1999: Alleviation of stationary biases in a GCM through a mountain drag parameterization scheme and a simple representation of mountain lift forces. *Mon. Wea. Rev.*, **127**, 788–801, https://doi.org/10.1175/1520-0493(1999)127<0788:AOSBIA>2.0.CO;2.

Lund, T. S., and D. C. Fritts, 2012: Numerical simulation of gravity wave breaking in the lower thermosphere. *J. Geophys. Res.*, **117**, D21105, https://doi.org/10.1029/2012JD017536.

Moin, P., K. D. Squires, W. H. Cabot, and S. Lee, 1991: A dynamic subgrid-scale model for compressible turbulence and scalar transport. *Phys. Fluids*, **3**, 2746–2757, https://doi.org/10.1063/1.858164.

Palmer, T. L., G. J. Shutts, and R. Swinbank, 1986: Alleviation of a systematic westerly bias in general circulation and numerical weather prediction models through an orographic gravity wave drag parametrization. *Quart. J. Roy. Meteor. Soc.*, **112**, 1001–1039, https://doi.org/10.1002/qj.49711247406.

Pautet, P.-D., and Coauthors, 2016: Large-amplitude mesospheric response to an orographic wave generated over the Southern Ocean Auckland Islands (50.7°S) during the DEEPWAVE project. *J. Geophys. Res. Atmos.*, **121**, 1431–1441, https://doi.org/10.1002/2015JD024336.

Portele, T. C., A. Dörnbrack, J. S. Wagner, S. Gisinger, B. Ehard, P.-D. Pautet, and M. Rapp, 2018: Mountain-wave propagation under transient tropospheric forcing: A DEEPWAVE case study. *Mon. Wea. Rev.*, **146**, 1861–1888, https://doi.org/10.1175/MWR-D-17-0080.1.

Reiss, J., and J. Sesterhenn, 2014: A conservative, skew-symmetric finite difference scheme for the compressible Navier–Stokes equations. *Comput. Fluids*, **101**, 208–219, https://doi.org/10.1016/j.compfluid.2014.06.004.

Sato, K., S. Watanabe, Y. Kawatani, Y. Tomikawa, K. Miyazaki, and M. Takahashi, 2009: On the origins of mesospheric gravity waves. *Geophys. Res. Lett.*, **36**, L19801, https://doi.org/10.1029/2009GL039908.

Schoeberl, M. R., 1985: The penetration of mountain waves into the middle atmosphere. *J. Atmos. Sci.*, **42**, 2856–2864, https://doi.org/10.1175/1520-0469(1985)042<2856:TPOMWI>2.0.CO;2.

Shoeybi, M., M. Svard, F. E. Ham, and P. Moin, 2010: An adaptive implicit-explicit scheme for the DNS and LES of compressible flows on unstructured grids. *J. Comput. Phys.*, **229**, 5944–5965, https://doi.org/10.1016/j.jcp.2010.04.027.

Smith, R. B., 2018: 100 years of progress on mountain meteorology research. *A Century of Progress in Atmospheric and Related Sciences: Celebrating the American Meteorological Society Centennial, Meteor. Monogr.*, No. 59, Amer. Meteor. Soc., https://doi.org/10.1175/AMSMONOGRAPHS-D-18-0022.1.

——, and Coauthors, 2016: Stratospheric gravity wave fluxes and scales during DEEPWAVE. *J. Atmos. Sci.*, **73**, 2851–2869, https://doi.org/10.1175/JAS-D-15-0324.1.

Smith, S., J. Baumgardner, and M. Mendillo, 2009: Evidence of mesospheric gravity-waves generated by orographic forcing in the troposphere. *Geophys. Res. Lett.*, **36**, L08807, https://doi.org/10.1029/2008GL036936.

——, S. L. Vadas, W. J. Baggaley, G. Hernandez, and J. Baumgardner, 2013: Gravity wave coupling between the mesosphere and thermosphere over New Zealand, *J. Geophys. Res.*, **118**, 2694–2707, https://doi.org/10.1002/jgra.50263.

Smolarkiewicz, P. K., and R. Rotunno, 1989: Low Froude number flow past three-dimensional obstacles. Part I: Baroclinically generated lee vortices. *J. Atmos. Sci.*, **46**, 1154–1164, https://doi.org/10.1175/1520-0469(1989)046<1154:LFNFPT>2.0.CO;2.

——, and ——, 1990: Low Froude number flow past three-dimensional obstacles. Part II: Upwind flow reversal zone. *J. Atmos. Sci.*, **47**, 1498–1511, https://doi.org/10.1175/1520-0469(1990)047<1498:LFNFPT>2.0.CO;2.

Taylor, M. J., P.-D. Pautet, N. R. Criddle, D. C. Fritts, S. D. Eckermann, S. M. Smith, G. Hernandez, and M. McCarthy, 2019: Large-amplitude mountain waves in the mesosphere observed on 21 June 2014 During DEEPWAVE: 1. Wave amplitudes, scales, momentum fluxes, and environmental sensitivity. *J. Geophys. Res. Atmos.*, **124**, 10 364–10 384, https://doi.org/10.1029/2019JD030932.

Vadas, S. L. 2007: Horizontal and vertical propagation, and dissipation of gravity waves in the thermosphere from lower atmospheric and thermospheric sources. *J. Geophys. Res.*, **112**, A06305, https://doi.org/10.1029/2006JA011845.

Wang, L., D. C. Fritts, B. P. Williams, R. A. Goldberg, F. J. Schmidlin, and U. Blum, 2006: Gravity waves in the middle atmosphere during the MaCWAVE winter campaign: Evidence of mountain wave critical level encounters. *Ann. Geophys.*, **24**, 1209–1226, https://doi.org/10.5194/angeo-24-1209-2006.

White, F. M., 1974: *Viscous Fluid Flow*. McGraw-Hill, 725 pp.